Inositol (1,4,5)-Trisphosphate Receptor Microarchitecture Shapes Ca^{2+} Puff Kinetics

Luis Diambra[†] and Jonathan S. Marchant[‡*]
[†]Laboratorio de Biología de Sistemas, Centro Regional de Estudios Genómicos, Florencio Varela, Buenos Aires, Argentina; and [‡]Department of Pharmacology, University of Minnesota Medical School, Minneapolis, Minnesota

ABSTRACT Inositol (1,4,5)-trisphosphate receptors (IP_3Rs) release intracellular Ca^{2+} as localized Ca^{2+} signals (Ca^{2+} puffs) that represent the activity of small numbers of clustered IP_3Rs spaced throughout the endoplasmic reticulum. Although much emphasis has been placed on estimating the number of active Ca^{2+} release channels supporting Ca^{2+} puffs, less attention has been placed on understanding the role of cluster microarchitecture. This is important as recent data underscores the dynamic nature of IP_3R transitions between heterogeneous cellular architectures and the differential behavior of IP_3Rs socialized into clusters. Here, we applied a high-resolution model incorporating stochastically gating IP_3Rs within a three-dimensional cytoplasmic space to demonstrate: 1), Ca^{2+} puffs are supported by a broad range of clustered IP_3R microarchitectures; 2), cluster ultrastructure shapes Ca^{2+} puff characteristics; and 3), loosely corralled IP_3R clusters (>200 nm interchannel separation) fail to coordinate Ca^{2+} puffs, owing to inefficient triggering and impaired coupling due to reduced Ca^{2+}-induced Ca^{2+} release microwave velocity (<10 nm/s) throughout the channel array. Dynamic microarchitectural considerations may therefore influence Ca^{2+} puff occurrence/properties in intact cells, contrasting with a more minimal role for channel number over the same simulated conditions in shaping local Ca^{2+} dynamics.

INTRODUCTION

Many cellular activities are controlled by changes in cytoplasmic free Ca^{2+} (1,2). One pathway for elevation of cytoplasmic Ca^{2+} is through the release of Ca^{2+} ions stored in the endoplasmic reticulum via inositol (1,4,5)-trisphosphate receptors (IP_3Rs). The activity of these intracellular Ca^{2+} channels is manifest as a spatiotemporal hierarchy of Ca^{2+} release events (3,4), encompassing openings of a single IP_3R (a Ca^{2+} blip: the unitary Ca^{2+} release event) and coordinated opening of clustered IP_3Rs (Ca^{2+} puffs: local Ca^{2+} release events most frequently visualized at low levels of stimulation in intact cells) through to global Ca^{2+} waves that result from macroscopic coordination of the activity of these individual Ca^{2+} release units (5).

Ca^{2+} regulation of IP_3R activity is crucial in orchestrating transitions throughout this continuum of Ca^{2+} release profiles. Most simplistically, the process of Ca^{2+} release from the ER through IP_3R can be considered nonlinear, as modest increases in cytosolic Ca^{2+} concentration favor channel opening allowing autocatalytic amplification in a process called calcium-induced calcium release (CICR) (6). For macroscopic Ca^{2+} signaling, neighboring Ca^{2+} release units become functionally coupled by Ca^{2+} diffusion and CICR to coordinate Ca^{2+} puffs into abortive and then propagating Ca^{2+} waves, depending on the levels of IP_3 (7–9). Ca^{2+} release is thought to be terminated by closure of IP_3Rs at higher Ca^{2+} concentrations established in the vicinity of active IP_3Rs. Ca^{2+} regulation of IP_3Rs is also sensitive to the time and context of ligand presentation (10–12), complicating an understanding at the microscopic level of factors that regulate triggering (initial IP_3R opening) and recruitment (coordination of neighboring IP_3R opening) of Ca^{2+} channels within individual IP_3R clusters within intact cells. Therefore, the variability of Ca^{2+} puff amplitude and duration at any given Ca^{2+} release site (4,13)—a consequence of the number and duration of IP_3Rs openings during a puff—reflects many factors impacting the formation and interpretation (sampling rate, kinetics, context) of the free Ca^{2+} profile evolving in the vicinity of clustered IP_3Rs (14–16).

One consideration that has not received much emphasis to date has been the role of Ca^{2+} puff-site microarchitecture in determining IP_3R activity and Ca^{2+} puff properties. The impact of IP_3R cluster ultrastructure has been largely overlooked owing to:

1. A paucity of structural data concerning Ca^{2+} release site architecture (5),
2. Results of key initial modeling studies that suggested IP_3R were closely packed at release sites (17), and
3. The prevailing assumption that experimental analyses of IP_3R microarchitecture at release sites would be precluded by optical resolution barriers.

Therefore, many theoretical models build on the computationally sparing assumption that IP_3R channels are in close contact (i.e., dimensionless models) such that Ca^{2+} concentrations are homogeneous throughout individual IP_3R clusters. However, a growing collection of experimental results suggest that Ca^{2+} puff sites may be composed of a loosely corralled organization of (active) IP_3Rs within a more dynamically malleable architecture than previous

Submitted July 2, 2010, and accepted for publication January 4, 2011.

*Correspondence: march029@umn.edu

Editor: Michael D. Stern.

0006-3495/11/02/0822/10 $2.00

doi: 10.1016/j.bpj.2011.01.003

thought (5). Notably, these data include the observation of propagating microwaves within individual Ca^{2+} puff sites (3,18) and the observation of Ca^{2+}-blip-like triggers preceding Ca^{2+} puffs at low levels of IP_3 (19). Of particular interest is a recent electrophysiological analysis showing that lone and clustered IP_3Rs show different channel behavior (14). These experimental data highlight the potentially varied impact of Ca^{2+} regulation within differentially organized IP_3R architectures beyond regulation of the triggering IP_3R. Clearly, the extent of sensitization and synchronization of neighboring IP_3Rs through CICR will be dependent on their separation within an individual Ca^{2+} puff site.

Several computational studies have considered the role of CICR at the ultrastructural level (17,20–24). The foundational study was the work of Swillens et al. (17), considering clusters of 20–30 IP_3Rs, which concluded that interchannel (pore-to-pore) distances as small as 12 nm were required to ensure effective IP_3R communication. In retrospect, with structural knowledge of the lateral dimensions of a single IP_3R (diameter ~ 20 nm, (25)), this theoretical prediction seems unreasonable. Subsequent studies of IP_3R clustering employed methods only adequate to emulate processes on the timescale of seconds (21), or on spatial scales suitable for modeling whole-cell Ca^{2+} signals (20), rather than approaches with spatiotemporal resolution sufficient for modeling Ca^{2+} puff dynamics (ms, nm resolution). Most relevant is the work of Shuai et al. (22), which focused on modeling Ca^{2+} dynamics at high resolution under physiologically realistic conditions. To estimate the number of IP_3Rs opening during a puff and the single channel current, the authors employed a model aligned with confocal linescan imaging data in the *Xenopus* oocyte incorporating mobile and immobile buffers, a fluorescent Ca^{2+} indicator, and a microscope point-spread correction. Their simulations adequately reproduce experimental linescan records when simulated Ca^{2+} puffs are generated by synchronous opening of 25–35 IP_3Rs distributed through a cluster of 300–800 nm, with a single channel current of ~0.4 pA (22). A more recent modeling study suggested a tighter average distribution of IP_3Rs (~450 nM (23)).

However, these models enforce synchronous opening of IP_3Rs, which persist as an open unit throughout the entire Ca^{2+} release event. Using these parameters as guidelines to minimize computational time, we have added stochastically gating ion channels into simulations within three-dimensional cytosolic space. By including the dynamics of IP_3R channel states into a computational model with high spatial and kinetic resolution, the dynamics of Ca^{2+} puff genesis can be simulated to address how IP_3R coupling efficiency and Ca^{2+} puff characteristics are impacted by IP_3R cluster ultrastructure. These simulations demonstrate that Ca^{2+} puffs can be supported by a loosely corralled architecture of clustered IP_3Rs, and that different microarchitectures impact Ca^{2+} puff kinetics. As such, these simulations suggest a viable and functionally malleable alternative to contact models of IP_3R clustering (14,17).

METHODS

Modeling physiological conditions in the cytoplasm

To model the impact of IP_3 receptor microarchitecture on Ca^{2+} puff properties, we employed a stochastic gating model for IP_3Rs within a realistic intracellular medium. In this model, Ca^{2+} released by IP_3Rs behaving stochastically, diffuses through a cytosolic volume (V) containing exogenous mobile buffer (EGTA), stationary buffer, and a fluorescent Ca^{2+} indicator (Fluo-4 dextran), with concentrations and properties as utilized previously (22,23). The chemical reactions of Ca^{2+} with these components were represented by

$$\left[Ca^{2+}\right] + [X] \underset{\beta_X}{\overset{\alpha_X}{\rightleftharpoons}} [XCa],$$

where $[X]$ represents the concentration of stationary buffer $[B_s]$, mobile buffer $[B_m]$, and fluorescent indicator $[F]$. The values α and β represent forward and backward binding rates, respectively, to individual buffer components.

Individual IP_3Rs were distributed uniformly within a square channel array ($N \times N$, where N is the number of IP_3Rs per line, and d is the minimum distance between channels) situated at the bottom of the modeled volume (plane $z = 0$), as shown schematically in Fig. S1 in the Supporting Material. To prevent finite size effects impacting modeling simulations, the modeled area was expanded by a boundary ($a = 2.6\ \mu$m). Tests using larger boundary values did not differ from the presented results. Furthermore, to minimize boundary effects on the simulations, we have used a periodic boundary condition in the lateral limits of the cuboid. The modeled volume therefore has dimensions $L \times L \times 5\ \mu$m (where $L = (N - 1) \times d + 2a$). Necessary simplifications were:

1. To consider the ER pool as a two-dimensional plane occupying no volume, but providing an infinite pool of releasable Ca^{2+},
2. To regard Ca^{2+} transport across the plasma membrane and ER Ca^{2+} uptake as kinetically irrelevant on the timescale of these simulations,
3. To assume that the diffusion coefficients of the Ca^{2+}-free and Ca^{2+}-bound forms of the indicator and mobile buffer were equal (26), and
4. To assume that the initial distribution total of the bound and free species is uniform.

Because Ca^{2+} is released through IP_3Rs into the cytoplasm, the dynamics of Ca^{2+} in the cytoplasm were governed by the equations

$$\begin{aligned}\frac{\partial[Ca^{2+}]}{\partial t} = {} & D_{Ca^{2+}}\nabla^2\left[Ca^{2+}\right] + \delta(x,y,0)\frac{O_{x,y}I_{ch}}{2F\delta V} \\ & + \beta_f[FCa] - \alpha_f[Ca^{2+}]\left([F]_T - [FCa]\right) \\ & + \beta_m[B_mCa] - \alpha_m[Ca^{2+}]\left([B_m]_T - [B_mCa]\right) \\ & + \beta_s[B_sCa] - \alpha_s[Ca^{2+}]\left([B_s]_T - [B_sCa]\right),\end{aligned} \tag{1}$$

$$\begin{aligned}\frac{\partial[FCa]}{\partial t} = {} & D_{FCa}\nabla^2[FCa] + \alpha_f\left[Ca^{2+}\right] \\ & \times \left([F]_T - [FCa]\right) - \beta_f[FCa],\end{aligned} \tag{2}$$

$$\begin{aligned}\frac{\partial[B_mCa]}{\partial t} = {} & D_{B_mCa}\nabla^2[B_mCa] + \alpha_m\left[Ca^{2+}\right] \\ & \times \left([B_m]_T - [B_mCa]\right) - \beta_m[B_mCa],\end{aligned} \tag{3}$$

$$\frac{\partial[B_sCa]}{\partial t} = \alpha_s\left[Ca^{2+}\right]\left([B_s]_T - [B_sCa]\right) - \beta_s[B_sCa], \qquad (4)$$

where $[X]_T$ represents total concentrations, D_X represents the diffusion coefficient of species X, $\delta(x,y,z)$ is the channel distribution function (value = 1 at a channel site, values = 0 otherwise), and F is the Faraday constant. I_{ch} is Ca^{2+} current of a single channel. $O_{x,y}$ is a random variable that represents the number of open channels at a specific site (x,y). In this article, with single channel resolution, $O_{x,y}$ can take only two values (1 when the channel is open and 0 otherwise). We did not consider subconductance states resulting from individual subunit opening. This assumption allowed the use of parameters estimated previously (22). Because the stationary buffer displays fast kinetics, we employed the rapid buffer approximation (see the Supporting Material (27,28)).

Kinetic model of IP_3-receptor

Given the small number of channels underlying the generation of Ca^{2+} puffs, it is necessary to consider binding processes involved in IP_3R activation as stochastic events. To model clustered IP_3Rs coupled by Ca^{2+} diffusion and CICR, we implemented a simple, stochastic version of the Othmer-Tang model (OTM) (29,30) to describe the kinetics of each individual IP_3Rs within the cluster. This IP_3R kinetic model specifies a binding site for IP_3, and one activatory site and one inhibitory site for Ca^{2+}. The kinetic rates values were selected to generate kinetic parameters in simulated Ca^{2+} puffs (Fig. 1) that were compatible with experimental data (7,8,19), recorded from the animal hemisphere of *Xenopus* oocytes. For example, the simulated Ca^{2+} puff in Fig. 1 has a rising phase of ~37 ms (at $N^2 = 49$ and $d = 90$ nm), compatible with experimental observations (milliseconds for trigger duration and Ca^{2+} puff rise-time (19)). The mean open dwell-time obtained with the simulated parameters was 6.8 ms (see Fig. S3), compatible with data from patch-clamp recordings of IP_3R channels in the oocyte nuclear envelope (mean open dwell-times in the range of 4–10 ms (31)).

The kinetic rates values used here (Table S1) are different from those originally proposed by Othmer and co-workers (29,30), because original values were chosen on the basis of steady-state data (32) rather than conditions relevant during the rising phase of a Ca^{2+} puff when IP_3Rs are responding to rapidly changing Ca^{2+} concentrations. Because *Xenopus laevis* oocytes are thought to express only one of the three vertebrate IP_3R isoforms (33), the model considers IP_3Rs as a homogenous population for simplicity. The initial channels state was assigned by considering a thermalization period for the channels immersed in cytosolic-like medium at constant IP_3, and where free Ca^{2+}, Ca^{2+} fluorescent indicator, and mobile and immobile buffer were previously set at the initial resting concentrations. At the start of this period, the sites of all channels are unoccupied and we simulated the kinetics of the receptors over 1 s, long enough for the configuration of channel state configuration to reach equilibrium. This channel state configuration was then set as the initial condition.

Simulation of Ca^{2+} puffs

The above kinetic model was embedded within physiologically realistic conditions to simulate Ca^{2+} puff genesis. Equations S5–S7 in the Supporting Material were numerically integrated using a Crank-Nicolson algorithm, with the actual configuration of open channels $O_{x,y}$ obtained from stochastic simulations of IP_3R kinetics. The volume V was gridded in small cells of volume $\delta V = \Delta x\Delta y\Delta$, where $\Delta x = \Delta y = 30$ nm, and $\Delta z = 0.25$–0.50 μm and the integration step was $\Delta t = 100$ μs. Simulations were performed to $N = 7$, 8, and 9 (i.e., 49, 64, and 81 channels in the cluster, respectively) and the distance between channels d ranged between 90 and 270 nm, based upon experimental estimates to limit computational demand.

The simulations initiate with a forced opening of a single IP_3R (positioned at the center of cluster) which then behaves stochastically. For

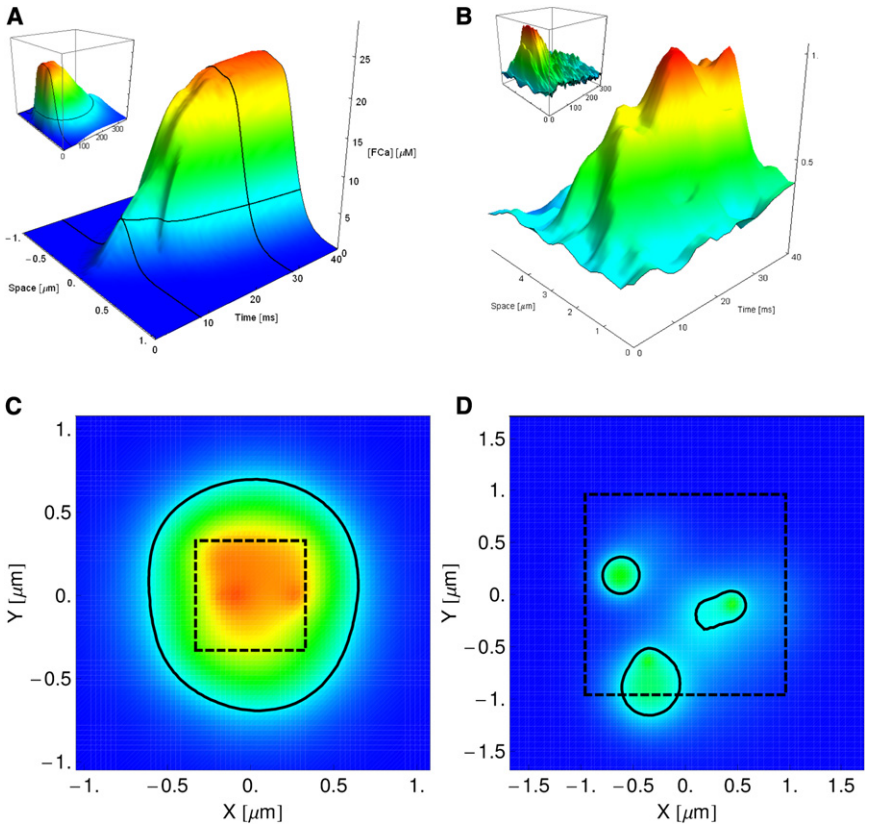

FIGURE 1 Graphical representation of the evolution of a Ca^{2+} puff. (*A*) The spatial evolution of the fluorescence profile along a scanline centered on the triggering channel every millisecond is plotted for 40 ms ($N^2 = 49$ and $d = 90$ nm) and the parameters of Table S1 in the Supporting Material. (*Horizontal line*) Amplitude (6.0 μM) threshold to be considered as a Ca^{2+} puff. The time separation between the *vertical lines* represents the duration over threshold (>20 ms) to be considered a Ca^{2+} puff. (*Inset*) The same Ca^{2+} release event but shown over a longer time course. (*Vertical line*) Duration of the main figure. (*B*) For comparison, an example of a Ca^{2+} puff recorded from a *Xenopus* oocyte plotted as shown in panel *A*. (*C* and *D*) Snapshot of two Ca^{2+} release events (*solid lines* represent the amplitude (6.0 μM) threshold; *dashed lines* are the area occupied spanned by the IP_3Rs). (*C*) Ca^{2+} puff generated by an IP_3R cluster with $d = 90$ nm, whereas disconnected events in panel *D* were generated by a cluster with the same number of IP_3Rs, but $d = 270$ nm. The Ca^{2+} release profile in panel *C* would be scored as a Ca^{2+} puff, whereas panel *D* would not.

each pair (N,d) of conditions, 20 stochastic simulations were performed. Two-dimensional snapshots (taken every 5 ms) of [FCa] over the ER membrane (i.e., $z = 0$) were processed (ImageJ, Ver. 1.37; http://rsbweb.nih.gov/ij/) using custom-written scripts based on the Analyze Particle toolbox to extract Ca^{2+} puff area, maximum amplitude, mean [FCa] values and position of the release events. We define Ca^{2+} puff area as the region where [FCa] > 6 μM. This definition is useful for modeling, but is not directly comparable with Ca^{2+} puff areas measured from experimental data due to the spread point function of the microscope. For all simulations (except Fig. 2 *B*, Fig. 6, and Fig. S2) [IP_3] was set at 500 nM.

Three criteria (amplitude, temporal, and spatial) were used to define whether a simulated response was identified—if all three criteria were met—as a Ca^{2+} puff:

1. Each snapshot was thresholded at 6.0 μM (amplitude filter).
2. Events with a lifetime of <20 ms at this threshold (Ca^{2+} blips) were disregarded from this population (temporal filter).
3. As a spatial filter for highly asynchronous responses, events in which the area of elevated fluorescence encompassed less than half the cluster area were excluded from analysis.

These criteria were defined by reference to an experimental dataset ($n = 330$ events) recorded from several donor frogs, by high-speed confocal imaging at multiple sites in the animal hemisphere.

Experimental measurement of Ca^{2+} puffs

Ca^{2+} puffs were recorded from *Xenopus* oocytes using methods described previously (see the Supporting Material). Ca^{2+} puffs were evoked by stimulation at a constant photolysis strength defined as 0.5 of the strength needed to trigger a propagating calcium wave (as (34,35)). Using the signal mass approach (4), events that comprised the smallest 5% of population values were identified as a population associated with the smallest extent of calcium release (likely comprising all blip events). The remaining events (95%) comprised the variable Ca^{2+} puff population (4). These same events were then reidentified in fluorescence profile, and all these events were found to lie below a threshold of 20% of the population mean peak fluorescence (equivalent to 6 μM in simulations), which was used as the amplitude threshold.

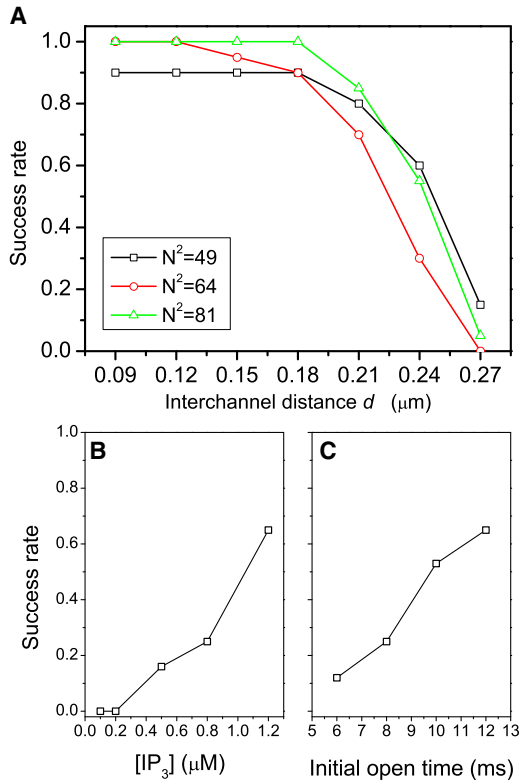

FIGURE 2 (*A*) Success rate (number of Ca^{2+} puffs observed divided by the number of simulations) as a function of interchannel distance d for N^2 49 (*squares*), 64 (*circles*), and 81 (*triangles*) IP_3Rs ([IP_3] = 0.5 μM.) (*B*) Success rate as a function of [IP_3] for $d = 270$ nm and $N^2 = 49$ IP_3Rs. (*C*) Success rate as a function of the initial open time at $d = 270$ nm, $N^2 = 49$ IP_3Rs, and [IP_3] = 0.5 μM.

Next, we filtered this population through a duration criterion derived from experimental records identifying Ca^{2+} blips. The majority of blips (>80%) had event durations <20 ms (Fig. 3 *C*). Therefore, any event with a duration of >20 ms above the amplitude threshold was likely a Ca^{2+} puff. Finally, we imposed a spatial synchrony criterion. This was necessary because a small number of simulated events scored as Ca^{2+} puffs were, however, clearly uncoordinated in their evolution. These were excluded from consideration as Ca^{2+} puffs, inasmuch as such events were never seen in experimental records. Likely they were a simulation artifact of the limited four-state model necessary as a computationally sparing simplification, which enforces transient reopening from inactivation before closure.

The following parameters were then measured from those signals fulfilling these three criteria and scored as Ca^{2+} puffs:

1. Success rate (number of puffs recorded divided by the number of trials);
2. Trigger duration (the time interval from the initial channel opening to Ca^{2+} puff threshold, i.e., 6.0 μM);
3. $T_{Area_{MAX}}$ (time to reach the maximum puff area); $T_{[FCa]_{MAX}}$ (the time to reach the peak of [FCa]);
4. The Ca^{2+} puff area relative to the cluster area;
5. The mean FCa concentration (averaged over the puff area); and
6. The propagation velocity of Ca^{2+} microwaves (3,18) observed within the cluster.

These values were obtained by averaging over 20 simulations performed with different random seeding variables.

RESULTS

Definition of a Ca^{2+} puff

Ca^{2+} puffs in *Xenopus* oocytes exhibit a broad range of kinetic profiles in experimental records, even when recorded at the same site (4). Therefore, a broad set of criteria was used to define a Ca^{2+} puff to encompass all synchronized, non-blip-like Ca^{2+} release events recorded from a simulated cluster. These parameters were used to compare Ca^{2+} puff dynamics between simulations (see Methods). Fig. 1 represents a graphical illustration of threshold criteria used to define a Ca^{2+} puff: amplitude ([FCa] > 6 μM), duration (>20 ms at [FCa] > 6 μM), and synchrony (area of elevated fluorescence [>20 ms at [FCa] > 6 μM] to be greater than half the cluster area). Fig. 1 *A* shows the same Ca^{2+} puff displayed over different timescales (40 vs. 300 ms) with these amplitude and duration filters demarked by solid lines.

This simulated profile is displayed alongside that of a Ca^{2+} puff recorded by linescan imaging in the *Xenopus* oocyte to underscore their kinetic similarity (Fig. 1 *B*). The broader spatial scale of the experimental Ca^{2+} puff compared to the simulated puff takes into account the point-spread function of confocal recording. Fig. 1, *C* and *D* (see Movie S1 and Movie S2 in the Supporting Material),

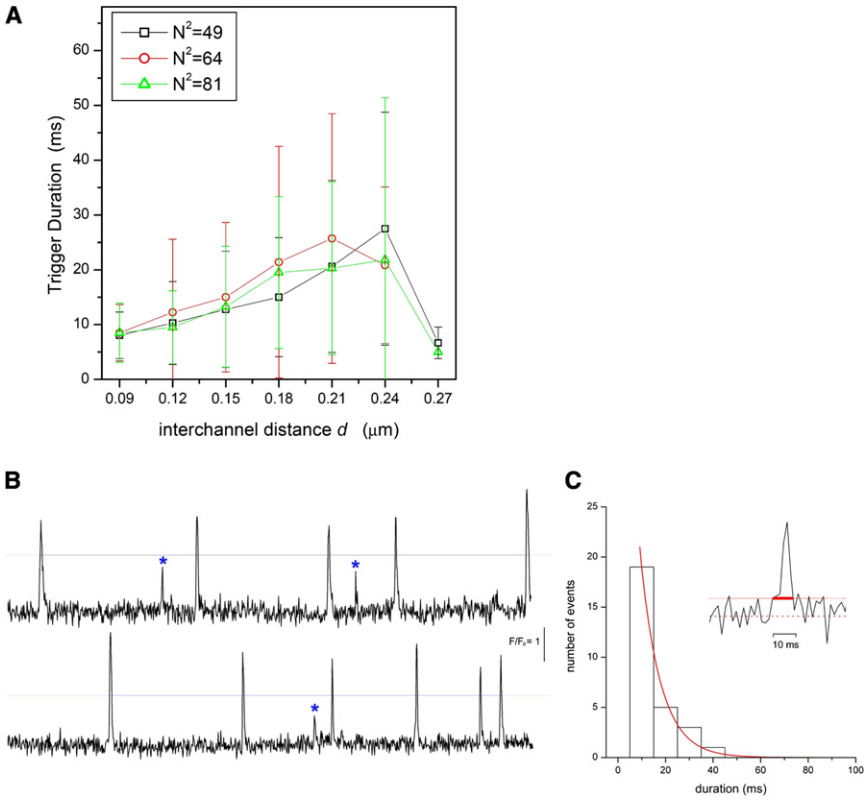

FIGURE 3 Kinetics of successful Ca^{2+} triggering events for different cluster architectures. N^2: 49 (*squares*), 64 (*circles*), and 81 (*triangles*). (*A*) Time interval from initial IP_3R opening to Ca^{2+} puff beginning (trigger duration) as a function of interchannel distance *d*. The curtailment of this trend at $d = 2.7$ μM reflects the observation that Ca^{2+} puffs were rarely observed at this condition as shown in Fig. 2. Error bars represent SD. (*B*) Fluorescence intensity traces recorded from two different Ca^{2+} puff sites, showing repetitive Ca^{2+} release activity. Intensity values were measured from a one-pixel region (0.2 μm) centered upon each Ca^{2+} puff site. (*Horizontal lines*) Fluorescence intensity ratio ($F/F_0 = 2.5$) below which smaller, isolated, sharp events were selected for processing (*asterisked*). (*C*) Histogram showing durations of Ca^{2+}-blip-like events. (*Inset*) Fluorescence intensity trace of one event to illustrate duration measurement (*thick bar*), defined as period for which intensity values exceeded noise threshold (*thin line*). This was defined as three standard deviations above average background intensities (*dashed line*, $F/F_0 \sim 1$) in the absence of Ca^{2+} release activity.

depicts examples of local Ca^{2+} release profiles that meet and fail the spatial synchrony criterion, respectively. Fig. 1 *C* shows a Ca puff where the area of elevated fluorescence (>6 μM) encompassed more than half the area of the cluster. Fig. 1 *D* shows an asynchronous response from a cluster of IP_3Rs where the area of thresholded amplitude remained less than half the cluster area. Such a response would not be classified as a Ca^{2+} puff.

Interchannel distance and puff genesis

To discern any impact of interchannel separation on Ca^{2+} puff dynamics, we first evaluated the success rate of individual IP_3R openings (Ca^{2+} blips) at triggering Ca^{2+} puffs. As a single IP_3R opens and closes stochastically, the resulting local Ca^{2+} change may not trigger a larger Ca^{2+} puff, as evidenced by the occurrence of isolated Ca^{2+} blips at Ca^{2+} puff sites in experimental records (4). We evaluated this success rate by resolving the ability of a single trigger (one initially open IP_3R which follows its own dynamics) to recruit neighboring IP_3Rs and elicit a Ca^{2+} puff at various simulated interchannel separations.

Fig. 2 *A* collates success rate (number of observed Ca^{2+} puffs divided by the total number of trials), as a function of varied IP_3R separation (*d*). These simulations:

1. Result in a variable success rate spanning from invariant Ca^{2+} puff occurrence to repeated failure as the interchannel separation is increased over a threefold range.
2. Show reliable Ca^{2+} puff triggering over narrow separations, which was maintained as IP_3R spacing was doubled (*d*, 0.09–0.18 μm). However, this was followed by an abrupt decline in triggering likelihood with invariant failure when channel separation increased only by a further 50% ($d \sim 0.18$–0.27 μm). The significance of the tipping point ($d > 0.20\mu$m) in terms of mechanistic explanations is explored further below.
3. Reveal that triggering of Ca^{2+} puffs is relatively independent of total IP_3R number (at least within this limited range, $N = 7$–9).

Therefore, Ca^{2+} puffs can be triggered effectively over a broad range of IP_3R cluster microarchitectures, a contrasting result to analyses that suggest close packing is required for invariant synchronization (<12 nm, for 90% synchronization; <50 nm, for 50% synchronization (17)).

Two further analyses of the success of Ca^{2+} puff triggering were performed.

First, as a control analysis, Fig. 2 *B* reports the dependency of Ca^{2+} puff triggering on $[IP_3]$, which was observed to span from zero probability at low $[IP_3]$ to consistent triggering as ambient $[IP_3]$ increased. More importantly, Fig. 2 *C* relates the duration of the initial IP_3R opening event to the success rate at recruiting neighboring channels, thereby triggering a Ca^{2+} puff using a fixed opening time for the initially active channel. A single IP_3R, opened for a fixed period (named initial open time 6–12 ms), then behaves stochastically. These simulations imply that

longer-duration triggers result in a higher probability of Ca^{2+} puff occurrence—a conclusion that we revisit below in relation to data from stochastic simulations and experimental measurements of Ca^{2+} blip lifetimes in the *Xenopus* oocyte.

To interpret the mechanistic basis for Ca^{2+} puff failure ($d > 0.20\ \mu$m), we then assessed the dynamics of Ca^{2+} puffs evoked over this range of cluster microarchitectures. The first parameter analyzed was trigger duration (the time interval from the initial channel opening to Ca^{2+} puff threshold, i.e., 6.0 μM), representative of the properties of the initial IP_3R opening that may trigger a Ca^{2+} puff. In these simulations, a trigger duration of ~10 ms at d ~ 100 nm was observed (Fig. 3 *A*). As interchannel distance was increased, the duration of the initial channel opening required to recruit neighboring IP_3Rs to form a Ca^{2+} puff lengthened (less than threefold) and this requirement for longer triggers was independent of the number of IP_3Rs in the cluster over the studied range. These simulations suggest more loosely corralled IP_3Rs architectures require longer Ca^{2+} triggers to effect intracluster recruitment of IP_3Rs.

Evaluation of this prediction was made through comparison with an experimental dataset of the smallest, isolated Ca^{2+} release events recorded at known Ca^{2+} puff sites. To do this, Ca^{2+} release events were identified in fast line scan experimental records that 1), were the smallest observed events ($F/F_0 < 2.5$; see mean of puff population $F/F_0 = 3.8 \pm 0.6$); 2), occurred in isolation; and 3), occurred at the same sites as Ca^{2+} puffs.

Fig. 3 *B* highlights examples of such events occurring from records at two different Ca^{2+} puff sites. The duration of these events was measured by quantifying the period of elevated fluorescence signal above background. Under typical conditions used to record elementary Ca^{2+} release events in the *Xenopus* oocyte, such Ca^{2+}-blip-like events are infrequently observed (4). Therefore, with the caveat that this dataset contains a small number of events ($n = 28$ events), the cumulative distribution histogram (Fig. 3 *C*) spans up to 40 ms, and can be adequately fit to a single exponential distribution with a time constant of 8.5 ms. These data therefore are in good agreement with the simulated mean channel open time (6.8 ms; see Fig. S3), and suggest that a low frequency of sufficiently long unitary Ca^{2+} release events (Fig. 3 *C*) contributes to the decrease in Ca^{2+} puff occurrence in broadly spaced IP_3R clusters (Fig. 2). Individual channels likely do not remain open long enough to impact Ca^{2+} sensitization of their neighbors in such loosely corralled IP_3R architectures and thereby summate into effective triggers.

Second, we analyzed the spatiotemporal properties of Ca^{2+} puffs from these different cluster organizations to derive insight to mechanisms delimiting Ca^{2+} puff properties once triggered. From the simulations, we sampled puff kinetics: time to reach the maximum area ($T_{Area_{MAX}}$), time to peak ($T_{[FCa]_{MAX}}$), puff amplitude, and spatial spread (Ca^{2+} puff area). The results of these simulations are shown in Fig. 4. At interchannel distance of 90 nm, Ca^{2+} puffs develop quickly as neighboring IP_3Rs open in a concerted manner with few Ca^{2+}-blip-like structures evident (Fig. 4, *A* and *B*, and Movie S1). This supports the approach of Shuai et al. (22), using a model assuming that channels open simultaneously. Increasing channel separation slowed the kinetics of Ca^{2+} puffs as reflected through a blunted rising phase where the time to peak ($T_{[FCa]_{MAX}}$) and time to reach the maximum area ($T_{Area_{MAX}}$) increased.

Consequently, the few Ca^{2+} puffs observed at $d = 270$ nm were slow to evolve and asynchronous channel activity was readily apparent (Movie S2). Relative puff area (i.e., spatial extent of the Ca^{2+} puff corrected for cluster size) and relative puff amplitude decreased as IP_3R separation increased, but neither of these parameters was significantly impacted by the number of clustered IP_3Rs. In summary, these simulations show that the smaller number of puffs observed at higher interchannel distances (Fig. 2) are characterized by smaller size (intensity and spatial spread) and slower kinetics of evolution of the Ca^{2+} release profile (Fig. 4, and Movie S1 and Movie S2). Ca^{2+} puff kinetics are, however, modulated by IP_3R organization over the range where Ca^{2+} puffs invariantly trigger, and at large interchannel distances where Ca^{2+} puffs recruitment fails, Ca^{2+} puff genesis is slower and more asynchronous.

At the high spatial-temporal resolution of this study, we were able to visualize Ca^{2+} microwave propagation within the cluster of IP_3Rs (Fig. 5 *A*) and thereby estimate the velocity of the interchannel Ca^{2+} wavefront through different IP_3R microarchitectures. This estimate was made by assuming the Ca^{2+} puff has cylindrical symmetry such that the radius at any time was represented by

$$r = \sqrt{Puff\ Area/\pi}.$$

The velocity of the interchannel Ca^{2+} wavefront propagation was then computed by linear fitting of the calculated radii as a function of time during the rising phase of the Ca^{2+} puff at different values of interchannel distance d (Fig. 5 *B*). This calculation demonstrated that the microwave velocity within the cluster decreased almost linearly as IP_3Rs separation (d) increased. Below the critical value ($d > 200$ nm) above which Ca^{2+} puff triggering fails (Fig. 2), microwave velocity decreased below a predicted value (<9 nm/ms) which was insufficient to synchronize neighboring IP_3Rs by intracluster CICR.

A final perspective on cluster microarchitecture derives from spatiotemporal probability plots. These representations depict the probability of finding an IP_3R (at distance x and time t) in an open (P_o) or inactivated (P_i) state after triggered channel opening. Fig. 6 shows spatiotemporal representations of $P_o(x,t)$ and $P_i(x,t)$ for IP_3Rs following the kinetic OTM at three decreasing concentrations of IP_3 (10 μM to 100 nM). After trigger channel opening ($t = 0$, $x = 0$ for 10 ms), probability distributions are established

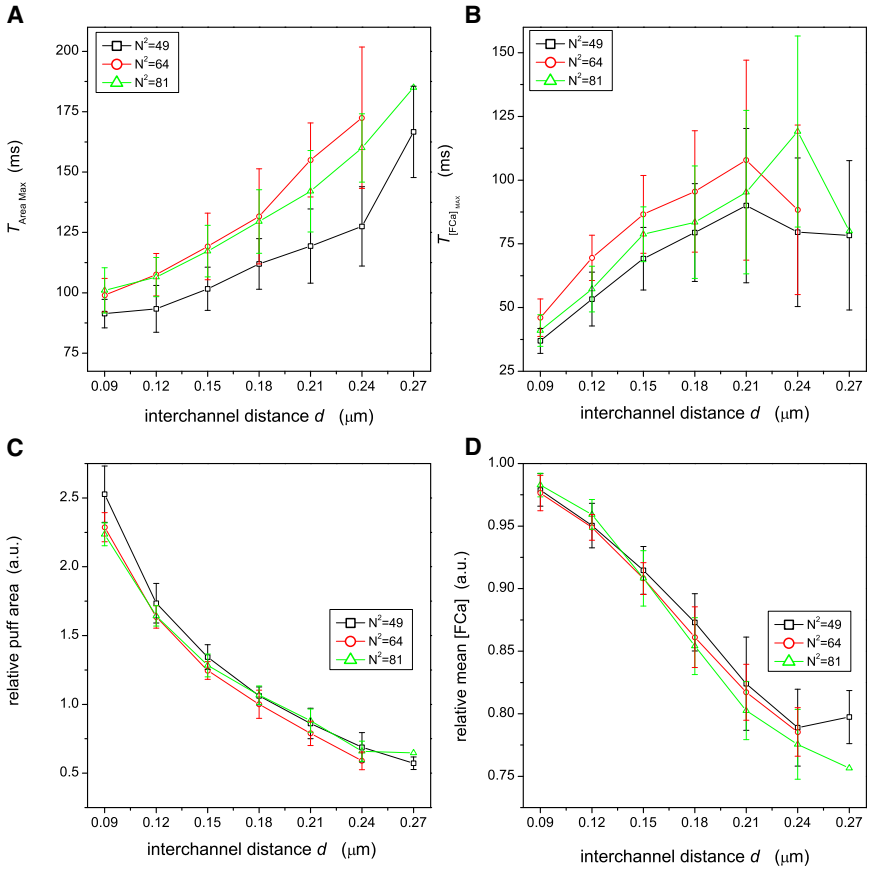

FIGURE 4 Puff characteristics for different number of clustered channels N^2: 49 (*squares*), 64 (*circles*), and 81 (*triangles*). (*A*) Time interval from initial trigger to maximum Ca^{2+} puff area ($T_{Area_{MAX}}$) as a function of interchannel distance *d*. (*B*) Time interval from initial trigger to the time when the maximum [*FCa*] ($T_{[FCa]_{MAX}}$) as a function of interchannel distance *d* is reached. (*C*) Mean area of puffs relative to the cluster area as a function of interchannel distance *d*. (*D*) Mean [*FCa*] of Ca^{2+} puffs, scaled by maximum [*FCa*] in all runs, as a function of interchannel distance *d*.

that define neighboring IP_3R states. Several features of these representations merit comment.

First, when following the basic OTM model, Ca^{2+} inhibition exerts a powerful, proximal cue for IP_3R inactivation. Ca^{2+} efflux from a neighboring channel effectively inhibits receptors within ~60 nm separation and recovery from inhibition is slow.

Second, the probability distribution for IP_3R opening is very different: the imprint is weaker, but broader and swifter than the corresponding P_i distribution. Therefore, Ca^{2+} release from the triggering IP_3R is able to immediately activate neighboring IP_3Rs with high probability (>0.8) over a broader area ($\leq$180 nm within 16 ms) accessed by inhibitory cues resulting from initial channel opening.

Third, comparison of the P_o and P_i distributions at the lower levels of IP_3 likely associated with elementary Ca^{2+} signaling, suggest that the maximal probability contour for IP_3R activation is spatially separated (~100 nm) from the trigger opening, whereas IP_3Rs proximal to the channel more likely occupy the inhibited state. This observation is compatible with the experimental observation of Ca^{2+} microwaves within a cluster (3,18), and the contention that a loosely corralled architecture of IP_3Rs within a Ca^{2+} puff site is an adequate, and indeed efficient way, to support local Ca^{2+} signals.

DISCUSSION

The discovery of local Ca^{2+} signals (i.e., Ca^{2+} puffs) resulting from IP_3R activity within the endoplasmic reticulum proved a key conceptual advance for understanding how IP_3-evoked Ca^{2+} waves trigger and propagate via summation of the discrete activity of clustered IP_3Rs (1,2). However, over the 20 years since these signals were first reported (36), comparatively little information has emerged concerning the microarchitecture of the IP_3R clusters that are spaced throughout the endoplasmic reticulum (5).

Are IP_3Rs tightly packed (contact models) at Ca^{2+} puff sites, or are IP_3Rs more broadly distributed (corral models) at active Ca^{2+} release sites?

Experimental evidence exists to support both models and neither iteration is necessarily exclusive, owing to the dynamic state of IP_3R organization within the endoplasmic reticulum (reviewed in (5)). Indeed this is well exemplified in the *Xenopus* system by the rapid changes in IP_3R architecture that occur during hormone-induced maturation, where IP_3R organization (35) and Ca^{2+} puff properties (37,38) become remodeled to prepare for the propagation of the fertilization Ca^{2+} transient (39).

The distinction between these models is, however, important—in so much as ultrastructural insight into cluster

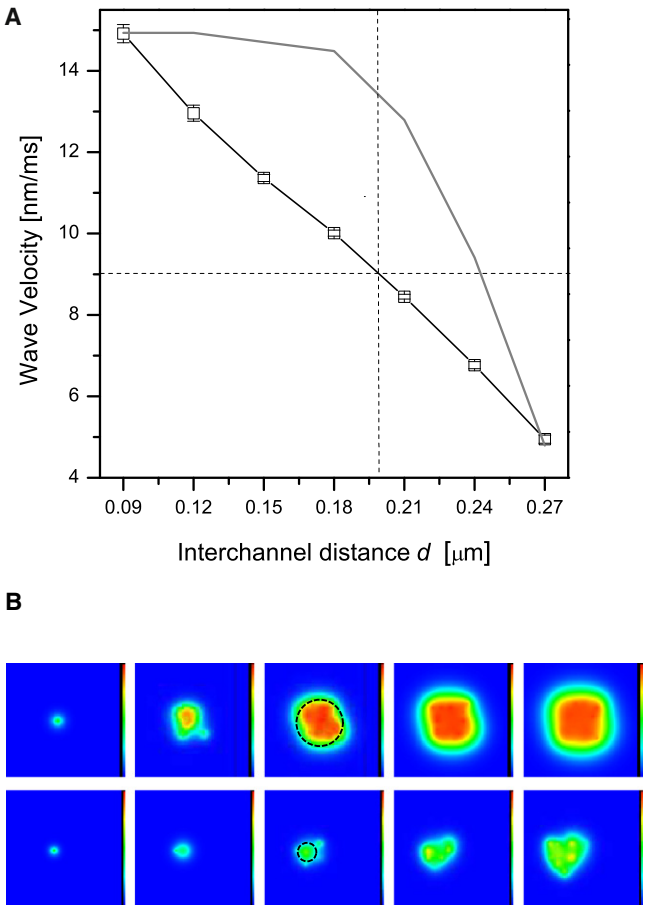

FIGURE 5 (*A*) Propagation velocity of Ca^{2+} microwave front as a function of interchannel distance *d*, for cluster size $N^2 = 49$. (*Dotted lines*) Approximates IP_3R separation above which Ca^{2+} puff occurrence decreases abruptly in simulations (~200 nm, from overlayed average from Fig. 2 *A*, in *gray*), corresponding to a Ca^{2+} microwave velocity of ~9 nm/ms. (*B*) Simulations of intracluster Ca^{2+} dynamics at different times after IP_3R opening (5 ms, 20 ms, 35 ms, 50 ms, and 65 ms, *left* to *right*) for cluster with intracluster distance *d* of 90 nm (*top*) and 210 nm (*bottom*).

organization impinges on several unknowns regarding IP_3R properties. These include the cell biological mechanisms that coordinate Ca^{2+} channel assembly/disassembly and delimit native cluster size, as well as providing crucial insight for understanding mechanisms of functional IP_3R recruitment. If IP_3Rs are closely packed at Ca^{2+} puff sites, then options such as conformational spread (between physically coupled Ca^{2+} channels (40)) or coordinated gating (through accessory protein spanning adjacent channel tetramers (41)) become viable models for interchannel communication, as alternatives to a coordinating role for Ca^{2+} feedback. More-sparsely distributed IP_3Rs would likely implicate by necessity Ca^{2+} feedback onto the cytosolic activatory sites of neighboring IP_3Rs as the mechanism for proximal IP_3R recruitment. However, the feasibility of supporting Ca^{2+} puffs through coordination of a small number of IP_3Rs within a loosely corralled microarchitecture to a high open probability is unclear.

For this very reason, we applied high-resolution modeling to investigate the impact of IP_3R microarchitecture on Ca^{2+} puff occurrence, by varying the organization of a fixed number of IP_3Rs within a single cluster. In contrast to several previous models, this approach incorporates stochastically gating IP_3Rs within a three-dimensional cytosolic space occupied by mobile and immobile Ca^{2+} buffers and the fluorescent Ca^{2+} indicator (17,21–24). Because of the computationally demanding nature of these simulations, we have initially restricted analysis to a limited number of IP_3Rs (49–81, as suggested by prior work (22)), a simple kinetic model of the IP_3R, and a static population of IP_3Rs (as an acceptable approximation over the timescale of these simulations). Nonetheless, the basic model reproduced Ca^{2+} puffs with kinetics similar to those observed experimentally (see Fig. 1) and a simulated mean channel open time (~7 ms; see Fig. S3) comparable with IP_3R mean open times (~8 ms (31)) recorded from isolated *Xenopus* nuclei.

These simulations predict Ca^{2+} puffs can be effectively triggered over a range of IP_3R architectures, with failure in interchannel coupling manifest only above >200 nm IP_3R separation (Fig. 2). From structural studies, we find that this value corresponds to a distance ~10-fold greater than the lateral dimensions of a single IP_3R (25). Therefore, from modeling insights alone, a corral-like organization with variable separation between individual IP_3Rs appears a viable alternative to a contact model (14) for IP_3R organization at Ca^{2+} puff sites. This conclusion contrasts with the foundational work of Swillens et al. (17), which predicted closer IP_3R coupling necessitated by a short effective range of Ca^{2+} feedback regulation.

This discrepancy may possibly be explained by the use of a rapid buffering approximation, or consideration of only the consequences of initial IP_3R triggering activity (17). However, our results are compatible with recent data (24) which approximated a distance of ~220 nm as a microscopic radius of influence for effective CICR (see below), as well as estimates of IP_3R cluster size greater than first thought (22,23). In terms of experimental evidence, the existence of unitary Ca^{2+} blips in both isolation (4) and as Ca^{2+} triggers at Ca^{2+} puff sites (19), the observation of saltatory Ca^{2+} microwaves within a IP_3R cluster (3,18), as well as the likelihood of large conformational movements between different IP_3R channel states (25,42) provide, on balance, further support for functionally coupled IP_3Rs existing within a more loosely corralled spatial architecture. Such an organization may even be a prerequisite for effective Ca^{2+} release activity (35).

What is the mechanistic basis for Ca^{2+} puff failure at larger (<200 nm) IP_3R separations? This results from a combination of ineffective triggering (Fig. 3) and a failure of subsequent amplification via CICR within the cluster—a failure of propagation (Fig. 5).

First, analysis of the triggering events that precede Ca^{2+} puffs demonstrated a requirement for progressively longer

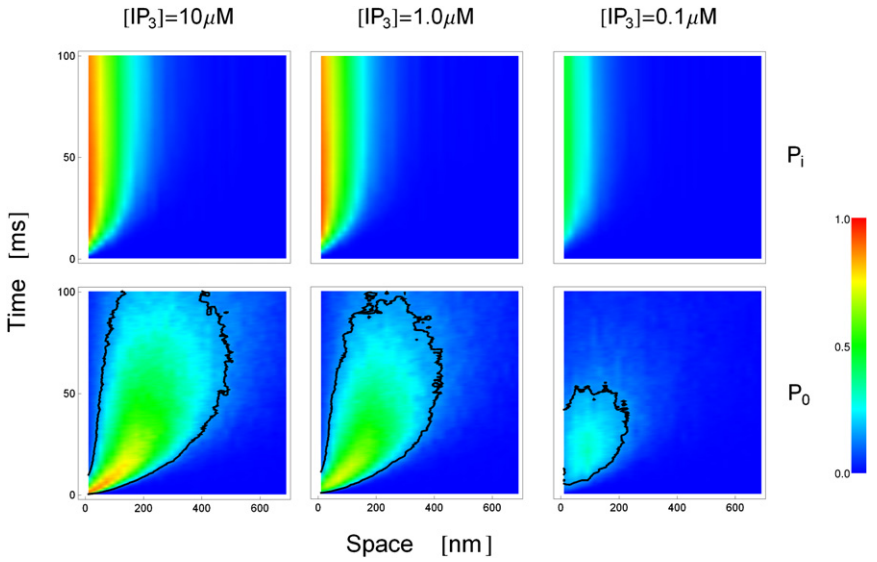

FIGURE 6 Spatiotemporal probability distribution, showing probability of finding a neighboring IP_3R in an open (P_o) or inactive (P_i) state at a distance (x) and time (t) subsequent to a triggered IP_3R opening (10 ms) at $t = 0$ and $x = 0$. Probabilities P_o (P_i) were computed by counting the number of probe channels (which do not release Ca^{2+} to the medium) in the open (inhibited) state at different positions and times. The simulation employed 1000 probe channels at each position. Probabilities are plotted on a pseudocolor scale for three different concentrations of IP_3 (10, 1, and 0.1 μM). (*Lower plot*, *solid contour line*) $P_o = 0.15$.

Ca^{2+} triggers to recruit proximal IP_3Rs as interchannel separation increases. In the simulations, a trigger duration of ~10 ms at $d \sim 100$ nm was observed (Fig. 3). This value is in good agreement with experimental measures of trigger duration (11.7 $\pm$ 0.7 ms (19) and the prediction of Shuai et al. (22) using a model enforcing synchronous IP_3R opening. This congruence implies a high degree of synchrony in IP_3R activity under such conditions. The need for progressively longer triggers as IP_3R separation increases needs to be rationalized in the context of the experimental distribution of Ca^{2+} blip duration recorded from *Xenopus* oocytes (Fig. 3 *C*). This distribution is a single exponential consistent with a single channel gating stochastically, and with comparatively few long-duration events (75% of events persist <20 ms). Consequently, the decline in Ca^{2+} puff triggering at >200 nm triggering is in part driven by a paucity of long-duration triggering events (>20 ms). Electrophysiological analysis of the mean *Xenopus* IP_3R open time reinforces that such long-duration unitary Ca^{2+} release events would occur only rarely (mean ~ 8 ms (31), see Fig. 3 *C*). The few Ca^{2+} puffs that occurred under these conditions (notably at $d < 270$ nm) resulted from fortuitous synchrony in channel opening (as reflected by the anomalous short trigger duration; see Fig. 3 *A*).

Second, CICR becomes less effective at synchronization as IP_3R channel separation increases. This is manifest through changes in Ca^{2+} puff kinetics, which become slower as individual IP_3R responses become asynchronous (Fig. 4). By visualizing microscopic CICR within the cluster, only abortive Ca^{2+} microwaves that dissipate between IP_3Rs are apparent at $d > 200$ nm (Movie S2). Measurements of the propagation of the Ca^{2+} microwavefront reveal a linear dependency on IP_3R separation and predicted that velocities of >10 nm/ms are required for effective recruitment of clustered channels under these modeling conditions. Obviously, changes in local buffering capacity will impinge on this relationship, consistent with observed experimental effects of exogenous Ca^{2+} buffers on the properties and coordination of elementary Ca^{2+} signals (15,16).

Third and finally, although considerable effort has been spent (re)estimating the number of IP_3Rs active during a Ca^{2+} puff, these simulations underscore that the kinetic profile of Ca^{2+} puffs is more impacted by IP_3R architecture than absolute IP_3R number over the studied range. Whereas IP_3R number in a cluster is clearly important in regulating puff frequency and absolute amplitude (23), subtle changes in IP_3R clustering—independent of changes in IP_3R number—can shape Ca^{2+} puff kinetics with sufficient malleability to have a role in regulating Ca^{2+} puff occurrence. Therefore, in parallel with debate over preformed (43) or induced formation of IP_3R clusters (14), the functional ramifications of cluster architecture itself should not be overlooked (44).

SUPPORTING MATERIAL

Three figures, one table, additional equations, and two movies are available at http://www.biophysj.org/biophysj/supplemental/S0006-3495(11)00045-2.

We thank Shuxia Zhang (Minnesota Supercomputing Institute) for help running simulations with MPI scripts. L.D. is a researcher at CONICET (Argentina).

This work was supported by the National Institutes of Health under grant No. GM088790 (to J.S.M.).

REFERENCES

1. Berridge, M. J. 1997. Elementary and global aspect of calcium signaling. *J. Physiol.* 499:291–306.
2. Bootman, M. D., P. Lipp, and M. J. Berridge. 2002. The organisation and functions of local Ca^{2+} signals. *J. Cell Sci.* 114:2213–2222.

3. Bootman, M. D., E. Niggli, …, P. Lipp. 1997. Imaging the hierarchical Ca^{2+} signaling system in HeLa cells. *J. Physiol.* 499:307–314.
4. Sun, X. P., N. Callamaras, …, I. Parker. 1998. A continuum of $InsP_3$-mediated elementary Ca^{2+} signaling events in *Xenopus* oocytes. *J. Physiol.* 509:67–80.
5. Diambra, L., and J. S. Marchant. 2009. Localization and socialization: experimental insights into the functional architecture of IP_3 receptors. *Chaos.* 19:37103.
6. Györke, S., and M. Fill. 1993. Ryanodine receptor adaptation: control mechanism of calcium induced calcium release in heart. *Science.* 260:807–809.
7. Marchant, J. S., N. Callamaras, and I. Parker. 1999. Initiation of IP_3-mediated Ca^{2+} waves in *Xenopus* oocytes. *EMBO J.* 18:5285–5299.
8. Marchant, J. S., and I. Parker. 2001. Role of elementary Ca^{2+} puffs in generating repetitive Ca^{2+} oscillations. *EMBO J.* 20:65–76.
9. Bootman, M. D., and M. J. Berridge. 1995. The elemental principles of calcium signaling. *Cell.* 83:675–678.
10. Finch, E. A., T. Turner, and S. M. Goldin. 1991. Calcium as a co-agonist of inositol 1,4,5-trisphosphate-induced calcium release. *Science.* 252:443–446.
11. Marchant, J. S., and C. W. Taylor. 1997. Cooperative activation of IP_3 receptors by sequential binding of IP_3 and Ca^{2+} safeguards against spontaneous activity. *Curr. Biol.* 7:510–518.
12. Adkins, C. E., and C. W. Taylor. 1999. Lateral inhibition of inositol 1,4,5-trisphosphate receptors by cytosolic Ca^{2+}. *Curr. Biol.* 9:1115–1118.
13. Thomas, D., P. Lipp, …, M. D. Bootman. 1998. Hormone-evoked elementary Ca^{2+} signals are not stereotypic, but reflect activation of different size channel clusters and variable recruitment of channels within a cluster. *J. Biol. Chem.* 273:27130–27136.
14. Rahman, T., A. Skupin, …, C. W. Taylor. 2008. Clustering of $InsP_3$ receptors by $InsP_3$ retunes their regulation by $InsP_3$ and Ca^{2+}. *Nature.* 458:655–659.
15. Dargan, S. L., and I. Parker. 2003. Buffer kinetics shape the spatiotemporal patterns of IP_3-evoked Ca^{2+} signals. *J. Physiol.* 553:775–788.
16. Dargan, S. L., B. Schwaller, and I. Parker. 2004. Spatiotemporal patterning of IP_3-mediated Ca^{2+} signals in *Xenopus* oocytes by Ca^{2+}-binding proteins. *J. Physiol.* 556:447–461.
17. Swillens, S., G. Dupont, …, P. Champeil. 1999. From calcium blips to calcium puffs: theoretical analysis of the requirements for interchannel communication. *Proc. Natl. Acad. Sci. USA.* 96:13750–13755.
18. Demuro, A., and I. Parker. 2008. Multi-dimensional resolution of elementary Ca^{2+} signals by simultaneous multi-focal imaging. *Cell Calcium.* 43:367–374.
19. Rose, H., S. L. Dargan, …, I. Parker. 2006. Trigger events precede calcium puffs in *Xenopus* oocytes. *Biophys. J.* 91:4024–4032.
20. Means, S., A. Smith, …, B. Wilson. 2006. Reaction diffusion modeling of calcium dynamics with realistic ER geometry. *Biophys. J.* 91: 537–557.
21. Shuai, J., and P. Jung. 2003. Optimal ion channel clustering for intracellular calcium signaling. *Proc. Natl. Acad. Sci. USA.* 100:506–510.
22. Shuai, J., H. Rose, and I. Parker. 2006. The number and spatial distribution of IP_3 receptors underlying calcium puffs in *Xenopus* oocytes. *Biophys. J.* 91:4033–4044.
23. Bruno, L., G. Soloveya, …, S. P. Dawson. 2010. Quantifying calcium fluxes underlying calcium puffs in *Xenopus laevis* oocytes. *Cell Calcium.* 47:273–286.
24. Solovey, G., and S. P. Dawson. 2010. Intra-cluster percolation of calcium signals. *PLoS ONE.* 5:e8997.
25. Wolfram, F., E. Morris, and C. W. Taylor. 2010. Three-dimensional structure of recombinant type 1 inositol 1,4,5-trisphosphate receptor. *Biochem. J.* 428:483–489.
26. Shuai, J., and I. Parker. 2005. Optical single-channel recording by imaging Ca^{2+} flux through individual ion channels: theoretical considerations and limits to resolution. *Cell Calcium.* 37:283–299.
27. Wagner, J., and J. Keizer. 1994. Effects of rapid buffers on Ca^{2+} diffusion and Ca^{2+} oscillations. *Biophys. J.* 67:447–456.
28. Stern, M. D. 1992. Buffering of calcium in the vicinity of a channel pore. *Cell Calcium.* 13:183–192.
29. Othmer, H. G., and H. Tang. 1993. Oscillations and waves in a model of calcium dynamics. *In* Experimental and Theoretical Advances in Biological Pattern Formation. H. Othmer, J. Murray, and P. Maini, editors. Plenum Press, London, UK. 295–319.
30. Diambra, L., and N. Guisoni. 2005. Modeling stochastic Ca^{2+} release from a cluster of IP_3-sensitive receptors. *Cell Calcium.* 37:321–332.
31. Mak, D. O., S. McBride, and J. K. Foskett. 1998. Inositol 1,4,5-trisphosphate activation of inositol trisphosphate receptor Ca^{2+} channel by ligand tuning of Ca^{2+} inhibition. *Proc. Natl. Acad. Sci. USA.* 95:15821–15825.
32. Bezprozvanny, I., J. Watras, and B. E. Ehrlich. 1991. Bell-shaped calcium response curves of Ins(1,4,5)P3- and calcium-gated channels from endoplasmic reticulum of cerebellum. *Nature.* 351:751–754.
33. Zhang, D., M. J. Boulware, …, J. S. Marchant. 2007. The inositol 1,4,5-trisphosphate receptor (ITPR) gene family in *Xenopus*: identification of type 2 and type 3 inositol 1,4,5-trisphosphate receptor subtypes. *Biochem. J.* 404:383–391.
34. Callamaras, N., J. Marchant, …, I. Parker. 1998. Activation and coordination of InsP3-mediated elementary Ca^{2+} events during global Ca^{2+} signals in *Xenopus* oocytes. *J. Physiol.* 509:81–91.
35. Boulware, M. J., and J. S. Marchant. 2005. IP_3 receptor activity is differentially regulated in endoplasmic reticulum subdomains during oocyte maturation. *Curr. Biol.* 15:765–770.
36. Parker, I., and Y. Yao. 1991. Regenerative release of calcium from functionally discrete subcellular stores by inositol trisphosphate. *Proc. Biol. Sci.* 246:269–274.
37. El-Jouni, W., B. Jang, …, K. Machaca. 2005. Calcium signaling differentiation during *Xenopus* oocyte maturation. *Dev. Biol.* 288:514–525.
38. Machaca, K. 2004. Increased sensitivity and clustering of elementary Ca^{2+} release events during oocyte maturation. *Dev. Biol.* 275:170–182.
39. Ullah, G., P. Jung, and K. Machaca. 2007. Modeling Ca^{2+} signaling differentiation during oocyte maturation. *Cell Calcium.* 42:556–564.
40. Yin, C. C., L. Blayney, and F. Lai. 2005. Physical coupling between ryanodine receptor-calcium release channels. *J. Mol. Biol.* 349: 538–546.
41. Marx, S. O., K. Ondrias, and A. R. Marks. 1998. Coupled gating between individual skeletal muscle Ca^{2+} release channels (ryanodine receptors). *Science.* 281:818–821.
42. Hamada, K., T. Miyata, …, K. Mikoshiba. 2002. Two-state conformational changes in inositol 1,4,5-trisphosphate receptor regulated by calcium. *J. Biol. Chem.* 277:21115.
43. Smith, I., S. Wiltgen, …, I. Parker. 2009. Ca^{2+} puffs originate from preestablished stable clusters of inositol trisphosphate receptors. *Sci. Signal.* 2:ra77.
44. DeRemigio, H., J. Groff, and G. Smith. 2008. Calcium release site ultrastructure and the dynamics of puffs and sparks. *Math. Med. Biol.* 25:65–85.